

Optimized Signal Estimation in Nanomechanical Photothermal Sensing via Thermal Response Modelling and Kalman Filtering

Hajrudin Bešić,^{1,*} Andreas Deutschmann-Olek,² Kenan Mešić,¹ Kostas Kanellopoulos,¹ and Silvan Schmid¹

¹*TU Wien, Institute of Sensor and Actuator Systems, Gusshausstrasse 27-29, 1040 Vienna, Austria*

²*TU Wien, Automation and Control Institute, Gusshausstrasse 27-29, 1040 Vienna, Austria*

(Dated: May 29, 2024)

We present an advanced thermal response model for micro- and nanomechanical systems in photothermal sensing, designed to balance speed and precision. Our model considers the two time constants of the nanomechanical element and the supporting chip, triggered by photothermal heating, enabling precise photothermal input signal estimation through Kalman filtering. By integrating heat transfer and noise models, we apply an adaptive Kalman filter optimized for FPGA systems in real-time or offline. This method, used for photothermal infrared (IR) spectroscopy with nanomechanical resonators and a quantum cascade laser (QCL) in step-scan mode, enhances response speed beyond standard low-pass filters, reducing the effects of drift and random walk. Analytical calculations show the significant impact of the thermal expansion coefficients' ratio on the frequency response. The adaptive Kalman filter, informed by the QCL's input characteristics, accelerates the system's response, allowing rapid and precise IR spectrum generation. The use of the Levenberg-Marquardt algorithm and PSD analysis for system identification further refines our approach, promising fast and accurate nanomechanical photothermal sensing.

I. INTRODUCTION

Nanomechanical resonators, pivotal for photothermal sensing through resonance frequency tracking, find extensive utility in fields such as infrared spectroscopy [1, 2] and broadband thermal infrared detection [3–9]. Demonstrated by these studies, nanomechanical photothermal sensing boasts low picogram and low picowatt sensitivity, respectively, without the need for cryogenic cooling. Nanomechanical photothermal sensing is applicable to diverse samples such as nanoparticles [10, 11], pharmaceutical compounds [2], and polymer thin films [12]. However, nanomechanical resonators face two primary challenges: i) a response speed typically ranging from 5 ms to 100 ms, creating an intrinsic trade-off between speed and precision; and ii) a step response dominated by two different transient responses, with the slower time constant often exceeding 100 seconds [13].

To address these challenges and enhance both the speed and precision of nanomechanical photothermal sensors, we develop a comprehensive thermal heat transfer and noise model, suited for optimal (Kalman) filtering. We test and apply the model and the Kalman-filter-based signal estimation by means of two experiments: one for model validation on a simple nanomechanical silicon-nitride string resonator, and another for conducting IR spectroscopy (NEMS-IR) on a more complex nanoelectromechanical drumhead resonator.

In the two experiments, we employ pulsed laser light in the visible and mid-IR range of the electromagnetic spectrum, respectively. The precise knowledge of the timing and shape of the input signal allows for adaptive Kalman filtering, significantly improving response speed compared to conventional low-pass filters. The designed Kalman filter estimates the input signal—specifically, the absorbed power—effectively by-passing the slow time constant characteristic of the measured

signal. Additionally, by incorporating the system's noise profile, the filtering process is optimized for greater accuracy. System identification was achieved through a parameter fitting algorithm applied to a step response, adjusting initial parameters to align the modeled response with the actual measurement data.

We show that the presented model and Kalman filtering effectively minimizes the influence of slow, undesirable processes such as drift and random walk, paving the way for fast, precise nanomechanical photothermal sensing.

II. METHODS

A. Experimental Setups

1. String Resonator Setup

To validate our model, we employ a nanomechanical silicon nitride string resonator, as shown in Figure 1a and detailed in prior work [14]. The resonator has a thickness of 56 nm, a width of 5 μm , and a length of 1 mm. It operates under a tensile stress of approximately 350 MPa, ensuring optimal performance within a vacuum environment maintained at a pressure below 10^{-5} mbar to minimize air damping effects. The resonance frequency of the device is recorded at around 170 kHz, accompanied by a high quality factor (Q) of $1.6 \cdot 10^6$ and a resonator time constant of 2.5 s. These parameters are integral to our experimental setup, providing a foundation for assessing the efficacy and accuracy of our proposed thermal heat transfer and noise model in a controlled environment.

The corresponding experimental setup is depicted in Figure 2a. It utilizes a laser diode (LPS-635-FC from Thorlabs GmbH) with a wavelength of 638 nm as the heating source. The laser diode is interconnected via an optical cable to an electro-optical modulator (EOM), which acts as a switch to create ideally shaped light pulses. The EOM is controlled by a

* hajrudin.besic@tuwien.ac.at

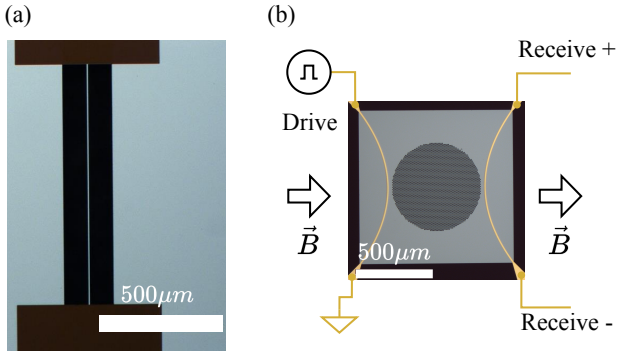


Figure 1. A microscope image of the nanomechanical resonators. (a) The silicon nitride string resonator. (b) The nanoelectromechanical drumhead resonator employed for infrared spectroscopy.

"Trigger" signal, which is connected to our FPGA-based electronics (PHILL from Invisible-Light Labs GmbH). From the EOM, the laser is directed through an optical cable to a laser-Doppler vibrometer (LDV) (MSA-500 from Polytec GmbH). The LDV focuses the probing laser beam onto the nanomechanical string resonator and simultaneously measures its motion using an additional readout laser with a wavelength of 633 nm. The readout signal is then transmitted via the "Receive" line back to PHILL. The string resonator is actuated using a piezo shaker, which is driven by PHILL through the "Drive" line.

2. NEMS-IR Setup

The NEMS-IR spectroscopy investigation employed a nanoelectromechanical resonator, which consists of a silicon nitride drumhead that is 50 nm thick and measures 1018 μm in length on each side, as detailed in prior work [15, 16] and depicted in Figure 1b. For the purpose of electrical transduction, the setup includes two gold electrodes, each being 5 μm in width, placed across the resonator. The system was positioned in a static magnetic field of about 0.8 T, produced by a Halbach array using neodymium magnets, with the electrode traces aligned perpendicularly to the field lines. This arrangement uses the Lorentz force, enabling one electrode to act as a driver by applying an alternating current, while the other electrode measured the resonator's movement via the induced voltage from magnetomotive forces. For signal detection enhancement, a differential pre-amplifier with a low noise profile and a gain of 10^4 was utilized. The drumhead resonator operated in a vacuum environment, maintaining a pressure of $1.6 \cdot 10^{-5}$ mbar. It exhibited a resonance frequency of $f_r = 134$ kHz, quality factor of 13 k and resonator time constant of 31 ms.

The experimental setup used to perform NEMS-IR is shown in 2b. Inside the chamber, the chip is placed between the magnets of the Halbach array and above the ZnSe window that is located at the bottom of the vacuum chamber. The chip electrodes are contacted with spring-loaded contacts. The read-

out electrode pins are connected to the differential pins of the preamplifier. The output of the preamplifier is connected to the "Receive" line. One pin of the drive electrode is connected to ground. To limit the high current flowing through the chip and prevent damage, the other pin is connected over an attenuator, with gain 10^{-3} , to the "Drive" line of the system.

To conduct NEMS-IR, we employ a tunable quantum cascade laser (QCL) as the laser source [1, 2]. Specifically, the MIRcat from Daylight Solutions laser is utilized, capable of generating up to 500 mW of average laser power and scanning the laser wave-number within a range of 1790 cm^{-1} to 1122.5 cm^{-1} . The laser's emission is focused onto the NEMS chip through a parabolic mirror and a ZnSe window. By sweeping the wave-number, the laser induces frequency detuning of varying magnitudes at different wave-numbers, thereby generating the IR spectrum.

The laser supports both continuous and step scan modes. In continuous mode, the laser remains activated while its wave-number is swept across the entire spectral range. Conversely, in step scan mode, the laser is set to a specific wave-number, activated, and after a predetermined hold time, deactivated and adjusted to a new wave-number. This sequence is reiterated until the full spectrum is covered. The step scan mode is preferred for its ability to generate a spectral sample by subtracting the "laser-off" frequency value from the "laser-on" value. Employing short sampling intervals allows for the suppression of slow processes such as thermal drift and random walk. The laser's state is synchronized with the PHILL frequency tracking device via the "Trigger" line, as illustrated in Figure 2b.

3. Frequency Tracking

The nanomechanical resonators are driven at their resonance frequency in a self-sustaining oscillator (SSO) resonance tracking scheme described in [15, 17]. The feedback of the SSO is realized with the PHILL, as schematically depicted in Figure 2. The feedback of the closed-loop SSO scheme is realized with phase and amplitude controlling elements to satisfy the Barkhausen criterion. The feedback consists of a band-pass filter whose main task is mode selection of the measurement mode and suppression of unwanted modes. After the band-pass filter, a comparator with 50 mV hysteresis is placed to detect edges and act as a 0-degree phase detector. The output of the comparator is connected to the pulse-generating mechanism that generates timed pulses with a pulse width T_w , delay relative to the detected phase of T_d , and an amplitude A , which can be between 3 V and -3 V. A frequency counter developed in [16] is used to acquire the frequency with a fixed sampling rate of around 20 kHz.

B. Thermal Response Model

The resonance frequency of a pre-stressed resonator is primarily influenced by the initial tension [18]. Variations in

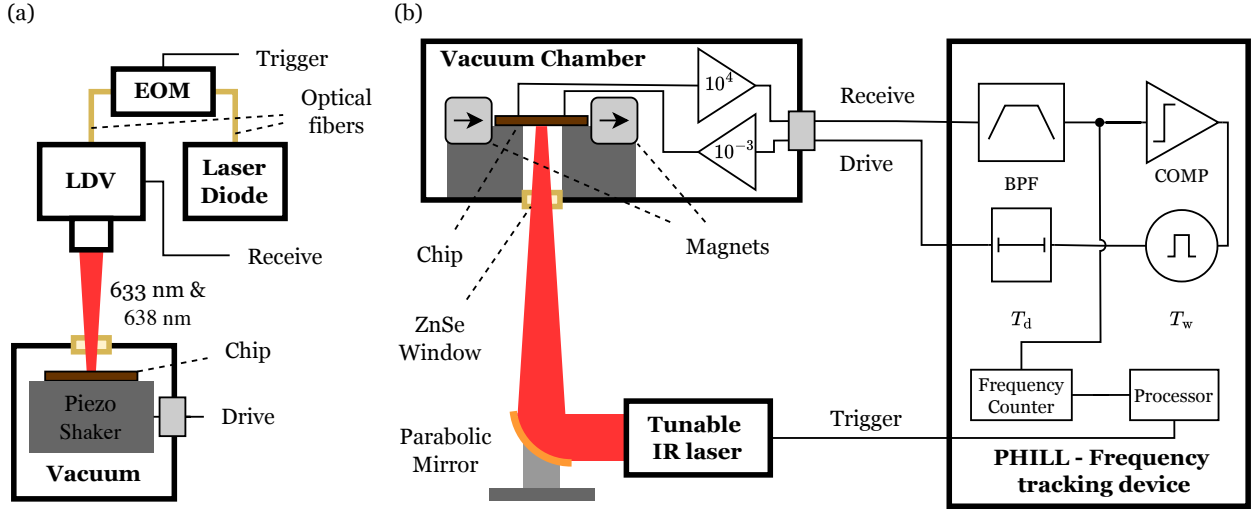


Figure 2. Schematic representation of the two measurement setups. Photothermal sensing with a) a nanomechanical string resonator in the visible and b) a nanoelectromechanical drumhead resonator to perform infrared spectroscopy NEMS-IR. Both setups are based on self-sustained frequency tracking with PHILL.

thermal expansion between the resonator and its supporting frame result in the resonator's strain being temperature-dependent, thereby inducing a temperature-dependent tensile stress. Consequently, the resonance frequency is also changed by temperature variations. Assuming a linear thermal expansion relationship for both the resonator and its frame, the temperature-induced strain in each of the two in-plane directions can be linearly approximated as [18]

$$\varepsilon = \varepsilon_0 - \alpha_r \Delta T_r + \alpha_f \Delta T_f \quad (1)$$

where ε_0 is the strain at the initial temperature T_0 without laser illumination, $\alpha_{r/f}$ are the coefficients of thermal expansion of the resonator/frame and $\Delta T_{r/f} = T_{r/f} - T_0$ are the difference between the resonator/frame and the initial temperature. Solving (1) for the temperature-dependent stress in each of the two in-plane directions, yields [19]

$$\sigma(T) = \sigma_0 - \frac{E}{1-\nu} (\alpha_r \Delta T_r - \alpha_f \Delta T_f) \quad (2)$$

where σ_0 is the stress at T_0 , E denotes Young's modulus, and ν is the Poisson's ratio. The fundamental mode eigenfrequency of a pre-stressed resonator can be calculated from the stress with the relation [18]

$$\omega_0 = \frac{\pi}{L} \sqrt{\frac{\sigma_0}{\rho} - \frac{E(\alpha_r \Delta T_r - \alpha_f \Delta T_f)}{\rho(1-\nu)}} \quad (3)$$

where L is the length and ρ the mass density of the resonator. For small changes in temperature, the equation can be approximated by the first-order Taylor approximation

$$\omega_0(T) \approx \omega_0(T_0) \left(1 - \frac{1}{2} \frac{E(\alpha_r \Delta T_r - \alpha_f \Delta T_f)}{\sigma_0(1-\nu)} \right) \quad (4)$$

In this simplified model, we ignore how temperature affects Young's modulus, thermal expansion coefficients, and mass density. However, in reality, a resonator's length and thermal expansion rates usually increase with temperature, while Young's modulus and mass density tend to decrease. However, these effects are negligible compared to the stress-change-induced frequency detuning. From the previous equation, the change in frequency caused by heating due to a change in temperature can be expressed as

$$\Delta \omega_0 = -\omega_0 g (\alpha_r \Delta T_r - \alpha_f \Delta T_f) \quad (5)$$

where g is a constant factor, which for a square drumhead is $g = E/[2\sigma_0(1-\nu)]$ and for a string with a uni-axial stress field reduces to $g = E/[2\sigma_0]$.

To utilize the static relation (5), the dynamics of ΔT_r and ΔT_f need to be described. Figure 3a shows the schematic representation of the heat flow of the chip. Operating in vacuum, there are two dominant types of heat flow in the system: conduction and radiation [20]. The resonator radiates heat on both sides and conducts heat over the frame into the environment. The heat flow can be approximated with a simple heat-transfer circuit diagram shown in Figure 3b. The thermal equivalent circuit model consists of the heat source P_a and thermal resistances and capacitances of the resonator, frame, and chip holder. The absorbed power P_a is calculated by multiplying the impinging power P_0 by the thermal absorption coefficient β , as expressed by the equation

$$P_a = P_0 \beta. \quad (6)$$

The heat flow due to radiation can be modeled as a heat source described by the Stefan-Boltzmann law [18, 20]

$$q_{\text{rad}} = 2\eta A_r \sigma_{\text{SB}} [(\Delta T_r + T_0)^4 - T_0^4]. \quad (7)$$

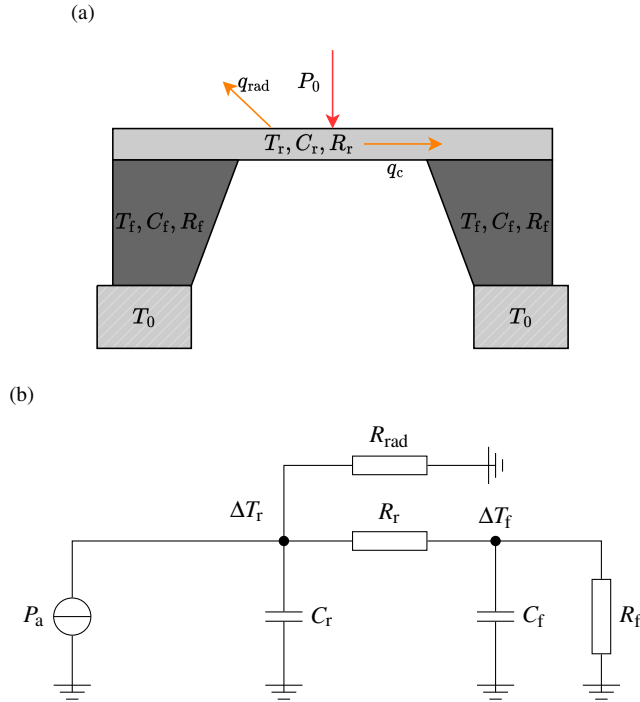


Figure 3. (a) Schematic of the different parts of the resonator and frame contributing to the thermal circuit model. (b) Linearized thermal equivalent circuit model of the resonator and frame and its thermal connection to the environment. (The ground symbol represents the environment temperature T_0)

For small temperature changes ΔT_r , the radiation can be linearized around T_0 and modeled as a thermal resistance to the environment with a constant thermal resistance

$$R_{\text{rad}} = \frac{\Delta T_r}{q_{\text{rad}}} = \frac{1}{8\eta A_r \sigma_{\text{SB}} T_0^3} \quad (8)$$

where η is the emissivity, A_r the surface of the resonator and T_0 the ambient temperature. From the thermal equivalent circuit model, a linear state-space model can be extracted as

$$\begin{bmatrix} \dot{\Delta T}_r \\ \dot{\Delta T}_f \end{bmatrix} = \underbrace{\begin{bmatrix} -\frac{R_r + R_{\text{rad}}}{R_r R_{\text{rad}} C_r} & \frac{1}{R_r C_r} \\ \frac{1}{R_r C_f} & -\frac{1}{R_r R_f C_f} \end{bmatrix}}_{\mathbf{A}_s} \begin{bmatrix} \Delta T_r \\ \Delta T_f \end{bmatrix} + \underbrace{\begin{bmatrix} \frac{1}{C_r} \\ 0 \end{bmatrix}}_{\mathbf{B}_s} P_a + \mathbf{w} \quad (9)$$

where \mathbf{A}_s is the dynamic matrix, \mathbf{B}_s the input matrix, \mathbf{x}_s the state vector, $\dot{\mathbf{x}}_s$ its derivative and \mathbf{w} the process noise in the system. From equation (5), the corresponding output equation of the state-space model can be formed as follows

$$\underbrace{\Delta \omega}_y = \underbrace{\begin{bmatrix} -\omega_0 g \alpha_r & \omega_0 g \alpha_f \end{bmatrix}}_{\mathbf{C}_s} \underbrace{\begin{bmatrix} \Delta T_r \\ \Delta T_f \end{bmatrix}}_{\mathbf{x}_s} + v \quad (10)$$

where \mathbf{C}_s is the output matrix of the system, y the measured quantity and v the measurement noise. The state-space model from equation (9) and (10) can be discretized in time [21] for

a chosen sampling time t_s which yields

$$\mathbf{x}_s(k+1) = \underbrace{e^{\mathbf{A}_s t_s}}_{\mathbf{F}_s} \mathbf{x}_s(k) + \underbrace{\int_0^{t_s} e^{\mathbf{A}_s \tau} \mathbf{B}_s d\tau}_{\mathbf{G}_s} P_a(k) + \mathbf{w}(k),$$

$$y(k) = \underbrace{\mathbf{C}_s}_{\mathbf{H}_s} \mathbf{x}_s(k) + v(k) \quad (11)$$

where \mathbf{F}_s is the discrete dynamic matrix, \mathbf{G}_s the discrete input matrix and \mathbf{H}_s is the discrete output matrix. The discrete state-space model (11) is particularly well suited for signal processing on digital systems.

III. NOISE MODELING AND KALMAN FILTERING

Noise modeling is a crucial aspect of Kalman filtering, an optimal estimation technique widely used in control systems, navigation, and signal processing [22, 23]. The primary goal of Kalman filtering is to estimate the state of a dynamic system from a series of noisy measurements. To achieve this, the Kalman filter relies on accurate models of both the system dynamics and the noise affecting the system. Specifically, the noise is categorized into two types: measurement noise and process noise, described by \mathbf{w} and v in equations (9) and (10). Measurement noise represents the errors in the observations [24, 25], while process noise accounts for the uncertainties in the system model itself [26]. The measurement variance (R) quantifies the expected errors in the measurements with the expected value $R(t - \tau) = \mathbb{E}[v(t)v(\tau)]$, and the process covariance matrix (\mathbf{Q}) characterizes the uncertainties in the system dynamics with the expected value $\mathbf{Q}(t - \tau) = \mathbb{E}[\mathbf{w}(t)\mathbf{w}^T(\tau)]$. These covariance matrices are essential for the Kalman filter to weigh the reliability of the predictions versus the new measurements correctly. By accurately modeling the noise, the Kalman filter can optimally combine information from the model and the measurements, resulting in precise and reliable state estimates. Understanding and implementing noise models is therefore fundamental to the effective application of Kalman filtering [27, 28]. In the following, we will describe the measurement and process noise of the system, disregarding slow processes such as drift and random walk. These slow noise processes are irrelevant because sampling occurs on much smaller timescales.

1. Measurement Noise

The measurement noise refers to the disturbances generated during the measurement of a specific physical quantity, in this instance, the temperature of the resonator. For a measurement performed in an SSO configuration two main noise contributors can be identified as shown in Figure 4: thermomechanical noise and detection noise. The thermomechanical noise is fundamental to nanomechanical resonators and can be modeled as white force noise acting on the resonator. This

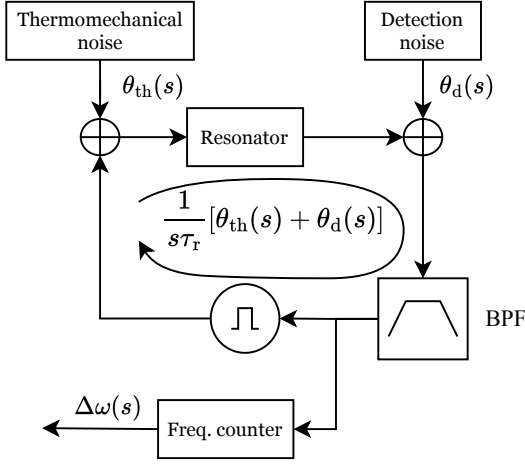


Figure 4. Noise contributions in the SSO frequency tracking scheme, represented in phase space

causes an amplitude noise to the position of the resonator at resonance with the power spectral density (PSD) [15, 17, 18] of

$$S_{\text{thm}} = \frac{4k_B T_r Q}{m\omega_0^3} \quad (12)$$

where k_B is Boltzmann constant, T_r the temperature, m the effective mass, ω_0 the eigenfrequency, and Q is the quality factor of the resonator.

Detection noise is produced by transducing the mechanical motion of the resonator into an electrical signal and is caused mostly by transduction and electronic noise. Being typically white Gaussian noise, detection noise PSD can be described with respect to the thermomechanical noise

$$S_d = \mathcal{K}^2 S_{\text{thm}}, \quad (13)$$

where \mathcal{K} is a dimensionless factor that corresponds to the ratio between the detection noise background and the height of the thermomechanical noise peak. The amplitude domain PSDs can be transformed into phase space by [17, 29]

$$\begin{aligned} S_{\theta_{\text{th}}} &= \frac{2}{A_r^2} S_{\text{thm}} \\ S_{\theta_d} &= \frac{2}{A_r^2} S_d = \mathcal{K}^2 S_{\theta_{\text{th}}} \end{aligned} \quad (14)$$

with the vibrational amplitude at resonance A_r .

The measurement noise sources contribute to the measuring noise in two different ways. The first is caused by phase detection noise passing through the band-pass filter (BPF), then through the low-pass filter of the frequency counter, and subsequently being transformed into frequency through differentiation. The second contributor is the closed-loop noise caused by the thermo-mechanical and detection noise combined. This type of noise is described by the Leeson effect [15, 17, 29], which asserts that within an SSO tracking scheme, phase noise is integrated and is proportional to the

reciprocal of the resonator's time constant τ_r , provided that it is significantly larger than the inverse of the band-pass filter's bandwidth. This integrated noise, after passing through the band-pass filter and frequency counter filter, is then differentiated and transformed into frequency. It can be described by white Gaussian thermo-mechanical noise passing through the transfer function G_v yielding the power spectral density

$$S_v(s) = |G_v(s)|^2 S_{\theta_{\text{th}}}(s), \quad (15)$$

with

$$G_v(s) = \frac{s\mathcal{K} + \frac{\sqrt{\mathcal{K}^2+1}}{\tau_r}}{(1+s\cdot\tau_{\text{BP}})(1+s\cdot\tau_{\text{FC}})} \quad (16)$$

where τ_{BP} represents the time constant of the band-pass filter, and τ_{FC} is the time constant of the frequency counter. Considering that the measurement noise follows a Gaussian distribution (even though it has not a constant PSD), a straightforward approach would be to empirically measure the noise variance and use

$$R = \sigma_v^2. \quad (17)$$

Literature [24, 30] suggests that a better approach for treating colored noise is to build a noise model based on its transfer function and augment it to the system in (9). The noise state space can be described in controllable canonical form as

$$\dot{\mathbf{x}}_v(t) = \underbrace{\begin{bmatrix} 0 & 1 \\ -\frac{1}{\tau_{\text{BP}}\tau_{\text{FC}}} & -\left(\frac{1}{\tau_{\text{BP}}} + \frac{1}{\tau_{\text{FC}}}\right) \end{bmatrix}}_{\mathbf{A}_v} \mathbf{x}_v(t) + \underbrace{\begin{bmatrix} 0 \\ 1 \end{bmatrix}}_{\mathbf{B}_v} u_v(t), \quad (18a)$$

$$v(t) = \underbrace{\begin{bmatrix} \frac{\sqrt{\mathcal{K}^2+1}}{\tau_{\text{BP}}\tau_{\text{FC}}} & \frac{\mathcal{K}}{\tau_{\text{BP}}\tau_{\text{FC}}} \end{bmatrix}}_{\mathbf{C}_v} \mathbf{x}_v(t), \quad (18b)$$

where u_v is the white measurement noise sequence with its auto-correlation $\mathbb{E}[u_v(t)u_v(\tau)] = S_{\theta_{\text{th}}} \delta(t-\tau)$, where $\delta(\cdot)$ is the Dirac delta function. The noise model can be discretized in time as shown in equation (11) yielding the discrete-time matrices \mathbf{F}_v , \mathbf{G}_v and \mathbf{H}_v .

2. Process Noise

The process noise represents the disturbances acting on the modeled states. In this model, it is epitomized by the temperature fluctuations exerted on the resonator. Temperature fluctuations are a fundamental phenomenon affecting all structures, primarily arising from the statistical and quantum aspects of heat exchange [31]. This process involves the absorption and emission of photons at the resonator surfaces, alongside thermal conduction to and from the surrounding environment via phonons. The resultant noise from this heat exchange manifests as shot noise, which exhibits white frequency noise behavior filtered by the resonator thermal response.

In the context the system described in (9), two temperature states are modeled: the resonator and the frame. The frame, due to its large size and very high thermal capacity, is assumed to have a static temperature with negligible fluctuations. Conversely, the resonator experiences significant temperature fluctuations, described by the spectral density [31]:

$$S_{\Delta T_r}(s) = \bar{S}_{\Delta T_r} |G_{\text{th}}(s)|^2 = 4k_B T_0^2 R_{\text{th}} |G_{\text{th}}(s)|^2, \quad (19)$$

where $R_{\text{th}} = R_r \parallel R_{\text{rad}}$ is the equivalent thermal resistance, and

$$G_{\text{th}}(s) = \frac{1}{1 + s \cdot R_{\text{th}} C_r} \quad (20)$$

is a first-order low-pass filter determined by the resonator's thermal properties. This behavior, when expressed in the controllable canonical state space form, can be articulated as follows

$$\dot{x}_w(t) = \underbrace{\left[\frac{1}{\tau_{\text{th}}} \right]}_{A_w} x_w(t) + \underbrace{\left[1 \right]}_{B_w} u_w(t), \quad (21a)$$

$$\mathbf{w}(t) = \underbrace{\begin{bmatrix} \frac{1}{\tau_{\text{th}}} \\ 0 \end{bmatrix}}_{C_w} x_w(t). \quad (21b)$$

where u_w is the white measurement noise sequence with its auto-correlation $E[u_w(t)u_w(\tau)] = \bar{S}_{\Delta T_r} \delta(t - \tau)$. The state space can again be discretized as shown in equation (11) yielding the discrete state space model F_w , G_w and \mathbf{H}_w . Combining the system dynamics (11) with the discretized colored noise models (18) and (21) yields

$$\mathbf{x}_s(k+1) = \mathbf{F}_s \mathbf{x}_s(k) + \mathbf{G}_s P_a(k) + \mathbf{H}_w x_w(k) \quad (22a)$$

$$x_w(k+1) = F_w x_w(k) + G_w u_w(k) \quad (22b)$$

$$\mathbf{x}_v(k+1) = \mathbf{F}_v \mathbf{x}_v(k) + \mathbf{G}_v u_v(k) \quad (22c)$$

$$y(k) = \mathbf{H}_s \mathbf{x}_s(k) + \mathbf{H}_v \mathbf{x}_v(k), \quad (22d)$$

resulting in a more comprehensive model that accounts for both measurement and process noise profiles.

A. Adaptive Kalman Filter

The fundamental speed versus accuracy limit of nanomechanical resonators is intrinsic. The accuracy can be improved by noise filtering, at the cost of speed reduction [15, 17]. However, this limit can be broken using additional information about the system. In the case of NEMS-IR using QCL step scan mode, it is known that the power input has a step shape with unknown height and known position in time (over the trigger in Figure 2). It can be modeled as an unknown but constant power with a small disturbance term w_{P_a} to introduce a form of uncertainty

$$P_a(k+1) = P_a(k) + w_{P_a}(k). \quad (23)$$

Through the thermal equivalent circuit model and equations (9) and (10), the dynamics of the system are also well

known. For problems of this type, an adaptive Kalman filter (AKF) can be used [32, 33]. Given the knowledge of the model, inputs, and stochastic properties of the system, it is capable of estimating the system in a statistically optimal manner [33]. Despite the knowledge of the input timing and shape the height of the absorbed laser power is unknown. Therefore, the model has to be extended and the Kalman filter needs to estimate in addition to the states the value of P_a . This can be achieved by augmenting the model [33], by adding (23) to the system (22) yielding

$$\underbrace{\begin{bmatrix} \mathbf{x}_s(k+1) \\ \mathbf{x}_v(k+1) \\ x_w(k+1) \\ P_a(k+1) \end{bmatrix}}_{\mathbf{x}(k+1)} = \underbrace{\begin{bmatrix} \mathbf{F}_s & 0 & \mathbf{H}_w & \mathbf{G}_s \\ 0 & \mathbf{F}_v & 0 & 0 \\ 0 & 0 & F_w & 0 \\ 0 & 0 & 0 & 1 \end{bmatrix}}_{\mathbf{F}} \underbrace{\begin{bmatrix} \mathbf{x}_s(k) \\ \mathbf{x}_v(k) \\ x_w(k) \\ P_a(k) \end{bmatrix}}_{\mathbf{x}(k)} + \underbrace{\begin{bmatrix} 0 & 0 & 0 \\ \mathbf{G}_v & 0 & 0 \\ 0 & G_w & 0 \\ 0 & 0 & 1 \end{bmatrix}}_{\mathbf{G}} \underbrace{\begin{bmatrix} u_v(k) \\ u_w(k) \\ w_{P_a}(k) \end{bmatrix}}_{\bar{\mathbf{w}}}, \quad (24a)$$

$$y(k) = \underbrace{\begin{bmatrix} \mathbf{H}_s & \mathbf{H}_v & 0 & 0 \end{bmatrix}}_{\mathbf{H}} \mathbf{x}(k). \quad (24b)$$

Notice that the measurement noise has been transferred from the output equation to the state equation. As a result, the system does not have measurement noise covariance matrix and all noise processes are described by the process noise covariance matrix. This matrix, described in the discrete time domain, is given by

$$\mathbf{Q} = \mathbb{E}[\bar{\mathbf{w}}\bar{\mathbf{w}}^T] = \begin{bmatrix} S_v t_s & 0 & 0 \\ 0 & \bar{S}_{\Delta T_r} t_s & 0 \\ 0 & 0 & \sigma_{P_a}^2 \end{bmatrix}. \quad (25)$$

where $\sigma_{P_a}^2$ is the process covariance matrix of the estimated absorbed power. The variance $\sigma_{P_a}^2$ is a tuning factor and has to be determined empirically. The Kalman filter algorithm is described in [32] and consists of the following steps

• Predict

$$\hat{\mathbf{x}}(k|k-1) = \mathbf{F}\hat{\mathbf{x}}(k-1|k-1), \quad (26a)$$

$$\mathbf{P}(k|k-1) = \mathbf{F}\mathbf{P}(k-1|k-1)\mathbf{F}^T + \mathbf{G}\mathbf{Q}\mathbf{G}^T, \quad (26b)$$

• Observe

$$\tilde{y}(k) = y(k) - \mathbf{H}\hat{\mathbf{x}}(k|k-1), \quad (26c)$$

$$\mathbf{V}(k) = \mathbf{H}\mathbf{P}(k|k-1)\mathbf{H}^T + \mathbf{R}, \quad (26d)$$

• Kalman gain

$$\mathbf{K}(k) = \mathbf{P}(k|k-1)\mathbf{H}^T \mathbf{V}^{-1}, \quad (26e)$$

• Estimate

$$\hat{\mathbf{x}}(k|k) = \hat{\mathbf{x}}(k|k-1) + \mathbf{K}(k)\tilde{y}(k), \quad (26f)$$

- Estimate covariance

$$\mathbf{P}(k|k) = (\mathbf{I} - \mathbf{K}(k)\mathbf{H})\mathbf{P}(k|k-1), \quad (26g)$$

where $\hat{\mathbf{x}}$ is the estimated state, \tilde{y} the difference between the measured and predicted state also called the innovation or residual, \mathbf{P} the covariance matrix of the state estimate and \mathbf{K} the Kalman gain. The notation $(n|m)$ means that at the corresponding quantity is estimated at a time n from the time m that is located in the past, i.e. $m \leq n$. The Kalman filter is a recursive algorithm used to estimate the state of a dynamic system from a series of noisy measurements. It combines predictions from a model with new measurements to produce an estimate that minimizes the mean of the squared error. The covariance matrix \mathbf{P} represents the uncertainty in the state estimate. It is updated at each step to reflect the confidence in the estimate.

When ever the laser is switched on or off, estimates of P_a from previous data are clearly becoming invalid. This can easily be included in the adaptive Kalman filter by manually increasing the covariance of the estimate \hat{P}_a (or even the whole covariance matrix \mathbf{P}). This way, the AKF adapts quickly to new measurement information at expense of more noisy estimates in the beginning. After a while the filter will converge back to its original filtering strength. The estimate of the impinging power \hat{P}_0 is obtained, by simply dividing the absorbed power estimate \hat{P}_a with the absorption coefficient of the structure β .

B. System Identification

Mathematical models are often derived from idealized scenarios and need to be calibrated to reproduce experimental data. In real world applications, factors like chip fabrication, laser alignment, or spot size of the laser illuminating the membrane can vary widely. Provided the system is linear, a step response system identification can be a powerful tool to properly characterize the different parameters of a dynamical system. The method of least squares is widely regarded as a simple and effective technique for extracting information from a dataset [34]. The method is optimal in the sense that the parameters determined by the least squares analysis are normally distributed about the true parameters with the least possible standard deviations.

The method of least squares is a parameter estimation method in regression analysis based on minimizing the sum of the squares of the residuals (a residual being the difference between an observed value and the fitted value provided by a model) made in the results of each individual equation. However, problems with this method can arise if the numerical algorithm gets stuck in a local minimum of the error function, resulting in suboptimal parameters. To prevent this from happening, in this case, initial parameters are roughly calculated analytically. They ensure that the numerical algorithm doesn't start too far from the global minimum, thus increasing its chances of finding the optimal solution. In this work, the *Levenberg–Marquardt* algorithm was used due to its robustness.

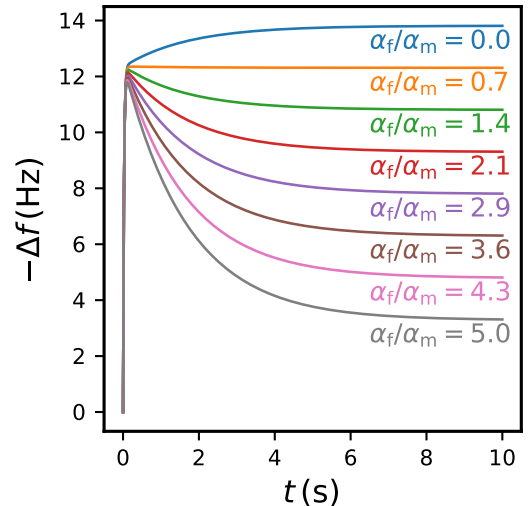


Figure 5. Step-responses of the system for different ratios of α_f and α_m .

IV. RESULTS AND DISCUSSION

Thermal systems that operate in a linear regime usually do not exhibit overshoots. It is mentioned in section II B that it is possible that the deformation of the frame can cause this effect due to its thermal expansion coefficient α_f . Figure 5 shows step responses generated for different ratios of the thermal coefficient of the membrane and frame. It can be seen that the slow frame-induced frequency shift does not have to always oppose the fast one. Usually, if $\alpha_f > c\alpha_m$ the frame expansion will oppose the fast frequency shift, and for $\alpha_f < c\alpha_m$ it will act in the same direction. In this case, $c \approx 0.7$ represents the equilibrium point where frame stretching and heating effects are balanced, resulting in a minimal impact on the response. It is important to note that, in theory, ratios exist where the effect of the frame can completely diminish initial membrane-induced frequency shift and at steady state $\Delta f = 0$. That means a mathematical configuration exists where the resonator acts as a high-pass filter. The other extreme theoretical case is when $\alpha_f = 0$. In this case the frame is not stretching and only heating. Then the steady-state value can be a lot larger than the initial jump from the fast process. This could be used as an advantage only if the drift of the sensor and other slow processes could be managed.

A. String Resonator Setup

In the first experiment, the performance of the model is evaluated. The thermal model is identified by fitting the parameters to a step response generated by a jump in laser power of $P_0 = 5.8 \mu\text{W}$. To fit the data, the initial parameters must be determined. In this work, we adopted a three-step approach for data fitting. Initially, we calculated the parameters analytically from the resonator geometry and material properties.

Subsequently, a manual fit of the parameters was performed, and in the final step, we ran the *Levenberg-Marquardt* algorithm to obtain the optimal parameters. Table I displays the values of the parameters obtained through data fitting, and Figure 6a shows the step responses for both the analytically calculated and fitted data.

The system's measurement noise is characterized by performing a 30s measurement at steady state with the laser turned off. The BPF 3dB bandwidth and the low-pass filter in the frequency counter are both set to 1kHz, chosen to be at least one order of magnitude larger than any transient phenomena in the system. The sampling rate of the frequency counter is set to approximately 20kHz. From the acquired data, a Power Spectral Density (PSD) is generated, as shown in Figure 6b. For better visualization, all PSDs are displayed in fractional frequencies. By fitting (15) to the PSD the measurement noise is calibrated to be $S_V = 5 \times 10^{-16} \text{ Hz}^{-1}$, while the thermal noise floor is calculated to be $\bar{S}_{\Delta T_r} = 6 \times 10^{-17} \text{ Hz}^{-1}$.

After the system is characterized by the step response and the noise by the PSD, the adaptive Kalman filter (AKF) can be employed. Figure 6c illustrates the AKF's response to a laser power jump of $P_0 = 5.8 \mu\text{W}$, induced by controlling the Electro-Optic Modulator (EOM). At the moment of the step, the covariance matrix of the AKF is increased by a factor greater than 10^4 , significantly expanding its bandwidth. This modification renders the system more sensitive to noise, resulting in a highly inaccurate initial estimate. Subsequently, the AKF swiftly decreases the bandwidth, allowing it to rapidly converge to a steady state. In this state, the measurement estimate aligns with the measurement signal trajectory, and the input estimate accurately reflects the step applied to the resonator. Figure 6d presents a closer view of the input step estimate's transient behavior, demonstrating that approximately 100ms to 200ms are required for the input estimate to stabilize at the input signal power value.

In the subsequent experiment, the reproducibility of the system is assessed. For three distinct power levels ($5.8 \mu\text{W}$, $15 \mu\text{W}$, and $25.6 \mu\text{W}$), the laser is alternately turned on and off five times, with a 50s interval between each sample. An estimate of the input power is collected 200ms after the laser event. Figure 6e displays the results, revealing that the system exhibits almost perfect linear behavior in both "on" and "off" states. The standard deviation among the samples is approximately 1% of the input power, underscoring the system's high reproducibility. This is particularly noteworthy considering the significant potential for drift and laser power fluctuations due to the lengthy intervals between sample acquisitions.

In the final experiment, the bias of the laser diode is adjusted to incrementally increase its output power in a step-wise manner. Altering the power in such a manner results in degradation of the step edges, attributable to the internal power regulation circuitry of the laser diode, which causes slow edges and edges with overshoots. As observed from Figure 6f, despite the transients not being perfectly consistent, the power estimation closely resembles a staircase function.

B. NEMS-IR Setup

At the outset of the experiment, it is imperative to characterize the model of the chip. Initially, the QCL is activated. Employing techniques described in Section III B, the transient step response is fitted to the measured data, as depicted in Figure 7a. Analysis of the data reveals two distinct time constants: a rapid transient in the positive direction and a markedly slower transient in the negative direction. To account for varying absorbance of the structures at different laser wavenumbers, all laser powers in the subsequent experiments will be normalized as

$$\tilde{P}_a = \frac{\hat{P}_a}{P_{1300}}, \quad (27)$$

where P_{1300} is the measured power at a wavenumber of $k = 1300 \text{ cm}^{-1}$ and \tilde{P}_a the normalized absorbed power estimate.

In the initial experiment, the QCL is set to a wavenumber of 1300 cm^{-1} with a power output of 0.45 mW. Upon activation, the laser illuminates the NEMS device, and the ensuing data are processed using both the Adaptive Kalman Filter (AKF) and a low-pass filter (LPF), with the cut-off frequency of 1 Hz, possessing a comparable filtering strength (approximately 0.4 Hz standard deviation over a 300ms recording period). As illustrated in Figure 7b, the data refined by the AKF exhibit a significantly quicker response compared to that processed by the low-pass filter. Upon detecting a jump, the Kalman filter's bandwidth expands substantially, facilitating a rapid response. Subsequently, the bandwidth narrows swiftly, and the data converge to a smoother curve that represents the optimal estimate. Figure 7b also reveals that the estimated absorbed power reacts the most promptly. For models that are both stable and reliable, the power estimate is deemed suitable. Note that any mismatch between the model and the actual experimental system may be mapped into wrong estimates by the AKF trying to reconcile model and measurements.

In the second experiment, the chip is coated with polystyrene, and data collection spans a duration of 3 minutes. The QCL operates in step scan mode, systematically covering the wavenumber range from 1789 cm^{-1} to 1122 cm^{-1} in increments of 1 cm^{-1} . For each wavenumber, the laser is activated for 100ms and subsequently deactivated for 150ms.

Figure 7c presents a section of the time-series data obtained from the scan. Notably, the input estimates rapidly converge to a stable, flat line. In contrast, the measurement estimate closely and smoothly tracks the measurement data. Although the low-pass filter succeeds in attenuating noise, it concurrently dampens the signal as well. This observation underscores the AKF's significant enhancement of the system's responsiveness. Utilizing a conventional low-pass filter necessitates a waiting period that is 5 to 10 times longer than the resonator's time constant to allow the signal to stabilize. A further complication arises due to frame stretching, which, influenced by a notably sluggish time constant, alters the signal. This effect complicates the determination of an optimal sampling point for the signal.

Parameter	g	C_r	R_{rad}	R_r	C_f	R_f	α_r	α_f
Calculation	357	$5.88 \cdot 10^{-10}$	$3.36 \cdot 10^8$	$1.48 \cdot 10^8$	$1.48 \cdot 10^{-7}$	$1.48 \cdot 10^8$	$1 \cdot 10^{-6}$	$1.6 \cdot 10^{-6}$
Fit	357	$2.39 \cdot 10^{-10}$	$3.1 \cdot 10^8$	$1.45 \cdot 10^8$	$6.88 \cdot 10^{-7}$	$2.6 \cdot 10^7$	$9.89 \cdot 10^{-7}$	$1.55 \cdot 10^{-6}$

Table I. Comparison between analytically calculated and fitted parameters.

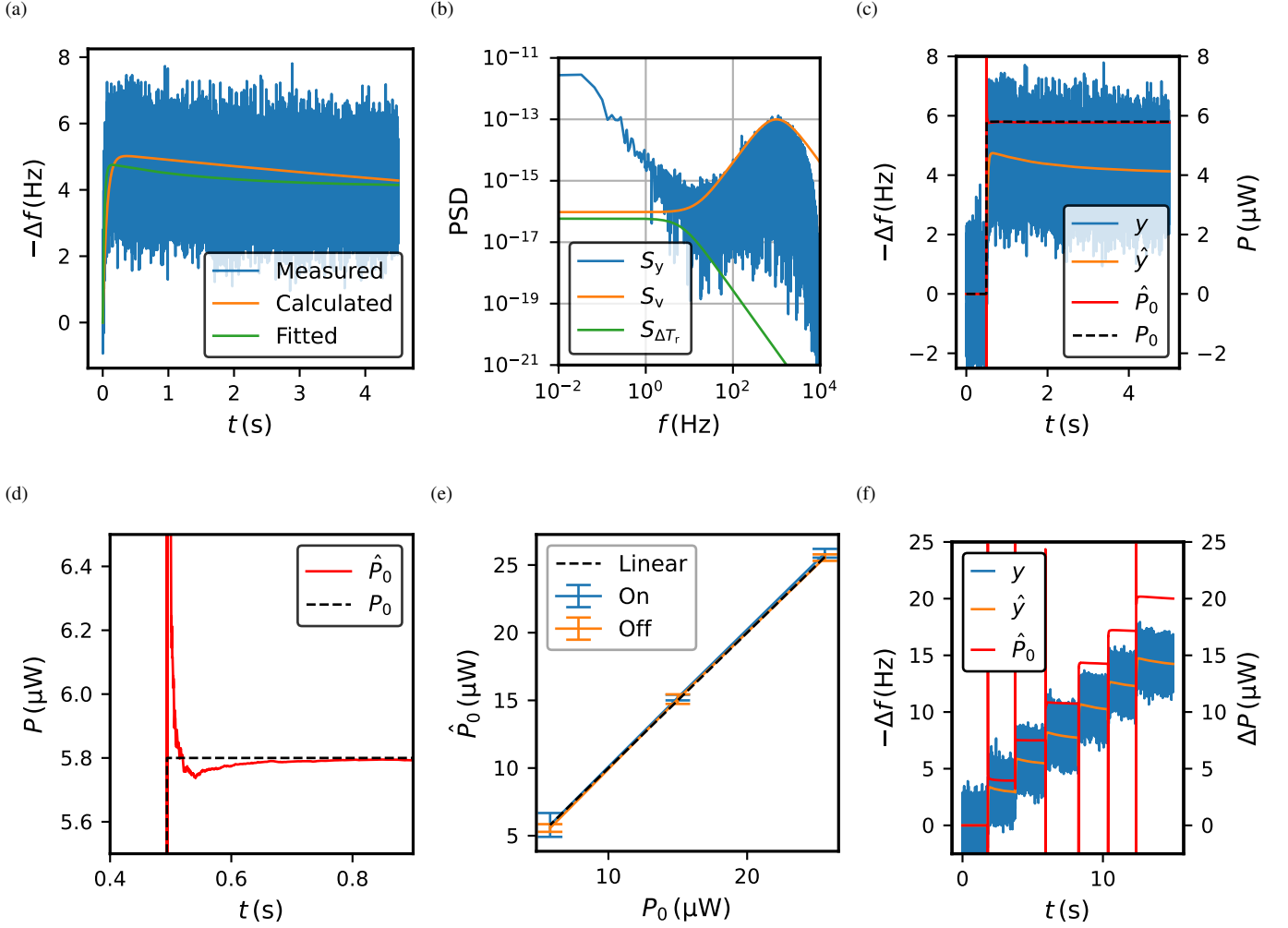


Figure 6. Results of the experiments performed on the string resonator: (a) System identification through calculation and subsequent fitting of the step response to the measured signal. (b) Characterization of measurement noise via the power spectral density of the measured signal, alongside a comparison with the calculated process noise. (Values are displayed in fractional frequency) (c) Visualization of the adaptive Kalman Filter estimates for a measured step response, contrasted against the input laser power to demonstrate stable and precise input power measurement. (d) A detailed view of the transient behavior in the power estimate, highlighting the significant initial estimate error and its rapid convergence to a steady state. (e) A reproducibility and linearity test conducted by executing 5 successive measurements across three power levels, including analyses of both "on" and "off" laser transients. (f) Application of the Adaptive Kalman Filter to a staircase function, showcasing immunity to the system's second slow time constant.

To generate the spectrum, data is collected differentially by subtracting consecutive measurements corresponding to the laser's on and off states. This method ensures that the resulting spectrum remains unaffected by slow noise processes, such as thermal drift and random walk processes. Figure 7d displays the resultant spectra for the AKF and LPF, which prominently feature the characteristic peaks of polystyrene. It can be observed that the spectrum generated by the AKF has

less noise and is cleaner, in comparison to the one generated by the LPF data.

V. CONCLUSIONS

In this study, we aimed to enhance the speed and precision of nanomechanical photothermal sensors by developing

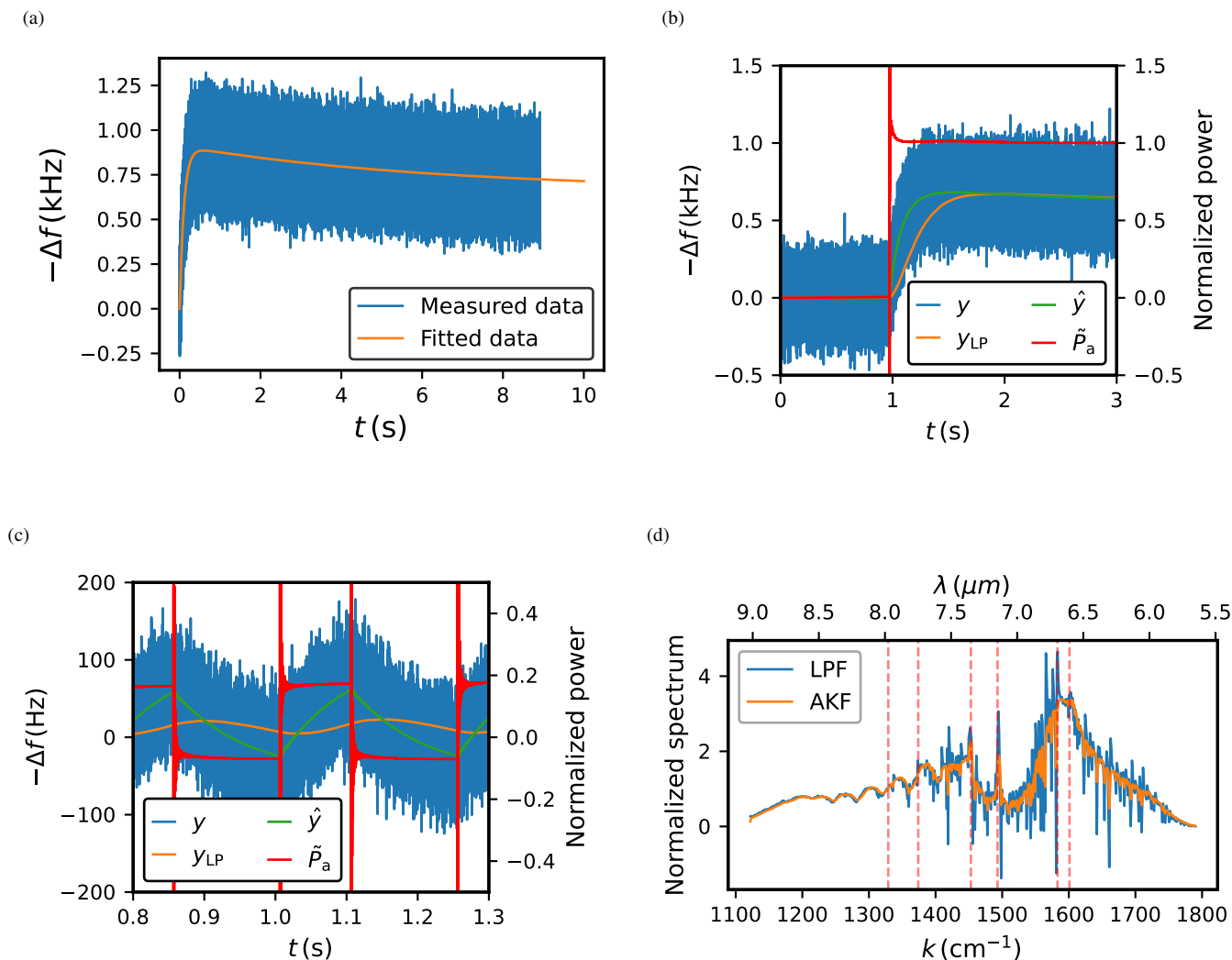


Figure 7. Results from the NEMS-IR experiments: (a) System identification for the NEMS-IR setup. (b) Adaptive Kalman filtering applied to a laser power step, illustrating a rapid power estimate, a comparatively slower measurement estimate, and an even slower response from a low-pass filter possessing equivalent filtering strength to the AKF. (c) A detailed view of a segment from the QCL step scan, comparing AKF and low-pass filter data. (d) Comparison of the polystyrene spectrum obtained using the adaptive Kalman filter estimate and the low-pass filter, with red lines highlighting the characteristic peaks. (some axes are inverted to provide an easier visualization)

a comprehensive thermal heat transfer and noise model suited for optimal Kalman filtering. We validated our model through experiments on a silicon-nitride string resonator and applied it to photothermal IR spectroscopy using a more complex nanoelectromechanical drumhead resonator.

Our thermal model accurately captures system dynamics, including the significant influence of the thermal expansion coefficients' ratio on the frequency response. The adaptable Kalman filter (AKF) we developed provides rapid and precise laser power estimation, suitable for real-time FPGA implementation or offline use. Experimental results demonstrated the model's accuracy and the AKF's effectiveness in managing measurement noise and maintaining stable power estimation.

In IR spectroscopy applications, the AKF enabled fast

data sampling and improved precision by eliminating slow time constant issues and successfully identifying characteristic spectral peaks. Overall, our comprehensive thermal model and Kalman-filter-based approach significantly advance the performance of nanomechanical photothermal sensors. The enhanced speed and precision achieved through this work offer promising avenues for further research and practical applications in the field of nanomechanical sensing. Future efforts will focus on refining the model and expanding its applicability to other resonator types and sensing modalities.

ACKNOWLEDGEMENTS

This work received funding from the European Innovation Council under the European Union's Horizon Europe Transition Open program (Grant agreement: 101058711-

NEMILIES). This project received funding from Defense Advanced Research Projects Agency (DARPA) Optomechanical Thermal Imaging (OpTIm) Technical Area (TA) 1 Broad Agency Announcement (BAA), HR001122S0055. The project received funding from the Novo Nordisk Foundation for the project MASMONADE with the grant reference number NNF22OC0077964.

-
- [1] N. Luhmann, R. G. West, J. P. Laffleur, and S. Schmid, Nanoelectromechanical infrared spectroscopy with in situ separation by thermal desorption: Nems-ir-td, *ACS sensors* **8**, 1462 (2023).
- [2] M. Kurek, M. Carnoy, P. E. Larsen, L. H. Nielsen, O. Hansen, T. Rades, S. Schmid, and A. Boisen, Nanomechanical infrared spectroscopy with vibrating filters for pharmaceutical analysis, *Angewandte Chemie* **129**, 3959 (2017).
- [3] M. Piller, J. Hiesberger, E. Wistrela, P. Martini, N. Luhmann, and S. Schmid, Thermal ir detection with nanoelectromechanical silicon nitride trampoline resonators, *IEEE Sensors Journal* **23**, 1066 (2022).
- [4] C. Zhang, E. K. Yalavarthi, M. Giroux, W. Cui, M. Stephan, A. Maleki, A. Weck, J.-M. Ménard, and R. St-Gelais, High detectivity terahertz radiation sensing using frequency-noise-optimized nanomechanical resonators, *arXiv preprint arXiv:2401.16503* (2024).
- [5] X. C. Zhang, E. B. Myers, J. E. Sader, and M. L. Roukes, Nanomechanical torsional resonators for frequency-shift infrared thermal sensing, *Nano Letters* **13**, 1528 (2013).
- [6] L. Duraffourg, L. Laurent, J. S. Moulet, J. Arcamone, and J. J. Yon, Array of resonant electromechanical nanosystems: A technological breakthrough for uncooled infrared imaging, *Micro-machines* **9**, 10.3390/mi9080401 (2018).
- [7] A. Blaikie, D. Miller, and B. J. Alemán, A fast and sensitive room-temperature graphene nanomechanical bolometer, *Nature Communications* **10**, 10.1038/s41467-019-12562-2 (2019).
- [8] L. Vicarelli, A. Tredicucci, and A. Pitanti, Micromechanical bolometers for subterahertz detection at room temperature, *ACS Photonics* **9**, 360 (2022).
- [9] C. Li, Y. Zhang, and K. Hirakawa, Terahertz detectors using microelectromechanical system resonators, *Sensors* **23**, 10.3390/s23135938 (2023).
- [10] S. Yamada, S. Schmid, T. Larsen, O. Hansen, and A. Boisen, Photothermal infrared spectroscopy of airborne samples with mechanical string resonators, *Analytical chemistry* **85**, 10531 (2013).
- [11] K. Kanellopoulos, R. G. West, and S. Schmid, Nanomechanical photothermal near infrared spectromicroscopy of individual nanorods, *ACS photonics* **10**, 3730 (2023).
- [12] A. Casci Ceccacci, A. Cagliani, P. Marizza, S. Schmid, and A. Boisen, Thin film analysis by nanomechanical infrared spectroscopy, *ACS omega* **4**, 7628 (2019).
- [13] A. T. Land, M. D. Chowdhury, A. R. Agrawal, and D. J. Wilson, Sub-ppm nanomechanical absorption spectroscopy of silicon nitride, *Nano Letters* (2024).
- [14] P. Sadeghi, M. Tanzer, S. L. Christensen, and S. Schmid, Influence of clamp-widening on the quality factor of nanomechanical silicon nitride resonators, *Journal of Applied Physics* **126** (2019).
- [15] H. Bešić, A. Demir, J. Steurer, N. Luhmann, and S. Schmid, Schemes for tracking resonance frequency for micro- and nanomechanical resonators, *Phys. Rev. Appl.* **20**, 024023 (2023).
- [16] H. Bešić, A. Demir, V. Vukićević, J. Steurer, and S. Schmid, Adaptable frequency counter with phase filtering for resonance frequency monitoring in nanomechanical sensing, *IEEE Sensors Journal* , 1 (2024).
- [17] A. Demir, Understanding fundamental trade-offs in nanomechanical resonant sensors, *Journal of Applied Physics* **129**, 044503 (2021).
- [18] S. Schmid, L. G. Villanueva, and M. L. Roukes, *Fundamentals of Nanomechanical Resonators*, 2nd ed. (Springer Cham, 2023).
- [19] E. Ventsel, T. Krauthammer, and E. Carrera, Thin plates and shells: theory, analysis, and applications, *Appl. Mech. Rev.* **55**, B72 (2002).
- [20] M. Piller, P. Sadeghi, R. G. West, N. Luhmann, P. Martini, O. Hansen, and S. Schmid, Thermal radiation dominated heat transfer in nanomechanical silicon nitride drum resonators, *Applied Physics Letters* **117** (2020).
- [21] R. Burns, *Advanced control engineering* (Elsevier, 2001).
- [22] R. E. Kalman, A new approach to linear filtering and prediction problems, *Journal of basic Engineering* **82**, 35 (1960).
- [23] G. Welch and G. Bishop, An introduction to the kalman filter, University of North Carolina at Chapel Hill, Chapel Hill, NC 7, 1 (1995).
- [24] R. G. Brown, *Introduction to random signal analysis and Kalman filtering* (Wiley New York, 1983).
- [25] A. Gelb, *Applied optimal estimation* (MIT press, 1974).
- [26] A. Ribeiro, Kalman and extended kalman filters: Concept, derivation and properties, in *Institute for Systems and Robotics, Instituto Superior Tecnico* (2004).
- [27] B. D. Anderson and J. B. Moore, *Optimal filtering* (Prentice-Hall Englewood Cliffs, NJ, 1979).
- [28] D. Simon, *Optimal state estimation: Kalman, H infinity, and nonlinear approaches* (John Wiley & Sons, 2006).
- [29] E. Rubiola, *Phase noise and frequency stability in oscillators* (Cambridge University Press, 2008).
- [30] D. C. Popescu and I. Zeljkovic, Kalman filtering of colored noise for speech enhancement, in *Proceedings of the 1998 IEEE International Conference on Acoustics, Speech and Signal Processing, ICASSP'98 (Cat. No. 98CH36181)*, Vol. 2 (IEEE, 1998) pp. 997–1000.
- [31] J. R. Vig and Y. Kim, Noise in microelectromechanical system resonators, *IEEE transactions on ultrasonics, ferroelectrics, and frequency control* **46**, 1558 (1999).
- [32] A. Demir, Adaptive time-resolved mass spectrometry with nanomechanical resonant sensors, *IEEE Sensors Journal* **21**, 27582 (2021).
- [33] M. Verhaegen and V. Verdult, *Filtering and system identification: a least squares approach* (Cambridge university press, 2007).

- [34] J. Wolberg, *Data analysis using the method of least squares: extracting the most information from experiments* (Springer Science & Business Media, 2006).